Integrated fusible alloy microelectrodes based microfluidic impedance cytometry for cell-in-droplet quantification

Jatin Panwar[1] and Rahul Roy[1,2,3#]

[1]Department of Chemical Engineering, [2]Centre for BioSystems Science and Engineering, [3]Molecular Biophysics Unit, Indian Institute of Science, Bangalore, India

[#]Correspondence:

Rahul Roy
Department of Chemical Engineering,
Indian Institute of Science, Bangalore,
Karnataka, India 560012
Telephone: +91-80-2293-3115;
Fax: +91-80-2360-8121
Email: rahulroy@iisc.ac.in;
rahulfx16@nanobiophotonics.org

Running title: Fusible alloy microelectrode impedance cytometry

Keywords: Microfabrication, Microelectrodes, Microfluidic impedance cytometry, Single cell analysis, Microdroplets.

Manuscript details:
Title – 104 characters; Short title – 44 characters; Abstract – 106 words; Text – 3498 words; Figures – 7; References – 60

1

Integrated fusible alloy microelectrodes based microfluidic impedance cytometry for cell-in-droplet quantification

Jatin Panwar[1] and Rahul Roy[1,2,3#]

[1]Department of Chemical Engineering, [2]Centre for BioSystems Science and Engineering, [3]Molecular Biophysics Unit, Indian Institute of Science, Bangalore, India

Microfluidic impedance cytometry (MIC) provides a non-optical and label-free method for single cell analysis. However, the cleanroom intensive infrastructure required for MIC electrode fabrication limits its implementation. As an alternate technique that enables rapid prototyping, we fabricated Field's metal 'in-contact' (icFM) coplanar microelectrodes in multilayer elastomer devices with a single photolithography step and characterised them for microfluidic impedance cytometry. Our icFM microelectrodes matched performance of the conventional platinum electrodes in the detection of single human erythrocytes and water-in-oil droplets in a feedback-controlled suction-flow MIC setup. Finally, to facilitate droplet based single cell analysis, we demonstrate detection and quantification of single erythrocytes entrapped in water-in-oil droplets.

I.   INTRODUCTION

Microfluidics allows precise control over chemical and biological investigations at micron scales enabling investigation of biological cells. As a result, microfluidic detection and analysis of single cells has seen a tremendous rise [1-3] and has been implemented in lab-on-chip and point-of-care applications.[4-7] In most microfluidic applications, cell detection is achieved using optical methods. Sensitive methods like fluorescence can allow molecule-specific detection enabling cell classification. However, these methods require additional labelling steps.[8] Therefore, there have been parallel efforts to develop label-free assays for the detection and characterization of cells.[9-12] One such promising technique is Microfluidic Impedance Cytometry (MIC) which relies on cellular electrical impedance.[13, 14] The dielectric properties of a cell are defined by characteristics like cell volume, composition and architecture. Continuous flow microfluidic devices with embedded microelectrodes for electrical measurements can be employed for detecting and classifying single cells in a high throughput manner.[14-18] In current versions of MIC, as the cell suspended in an electrolyte flows over an array of metal electrode pairs connected to a high frequency AC excitation source, the dielectric properties of the media between the electrodes change. This attenuates the measured impedance at a particular frequency across the microelectrode pair and generates a peak in the differential output. MIC based detection has already been employed in characterization of sub-cellular features.[14, 15, 19]

However, MIC devices rely on cleanroom intensive techniques like metal sputtering/vapour deposition to generate metal electrodes on substrates (glass or silicon wafer). The substrate is then bonded to the flow channel to complete the assembly of a coplanar microelectrode integrated microchannel.[20-22] This two-stage and costly microelectrode device fabrication process has limited the deployment of MIC in diagnostics and real-world applications.

There have been several prior efforts to develop cheaper and efficient embedded microelectrodes. For example, fusible alloy or liquid metal can be filled into dedicated microchannels placed in proximity with flow-channels to act as non-contact electrodes.[23, 24] However, these electrodes have limited impedance sensitivity due to attenuated charge density and electric field strength between the electrodes with the intervening elastomer. As impedance sensitivity has a strong dependence on electrode dimensions and displays optimum sensitivity for electrode widths comparable to the particle size,[25, 26] fabrication of microelectrodes and their placement in close proximity to flow channels is critical for MIC. To address this, alternate architecture(s) where the electrodes are in direct contact, namely, 'in-contact' with the flow channel are employed [27-30]. Even though

the applicability such embedded microelectrodes for impedance detection of single biological cells have been shown before,[30] their stability and their performance relative to conventional electrodes has not been characterized previously. Further, such electrodes have not been used for single cell analysis in multiphase microfluidic systems.

In this work, we present a simple fabrication method and characterization of MIC compatible coplanar 'in contact' Field's metal (icFM) microelectrodes. Our icFM microelectrodes displayed impedance signal strengths and contrast that is comparable to the conventional platinum electrodes for single erythrocyte detection in a custom-built suction driven continuous flow setup. After establishing the stability and compatibility of icFM with MIC, we used the setup for single cell quantification in droplets, a requisite for many single cell analysis platforms.[31-33] Our method provides a label-free non-optical approach to detect and quantify cells within water-in-oil microdroplets unlike some previous attempts.[34, 35] Therefore, our icFM integrated microelectrodes based MIC is a low-cost alternative for microfluidic single cell analysis.

II. MATERIALS AND METHODS

A. Electrode fabrication

Microchannels for the flow and the microelectrode layers were designed and fabricated using standard soft photolithography methods.[36, 37] Briefly, microchannels were designed using CleWin 4 and the chrome mask was etched using a mask writer (Heidelberg μPG 501) and EVG 620 was used for UV exposure. Polydimethylsiloxane or PDMS (184 Sylguard, Dow Corning) was used for all the device fabrications. SU8 2015 (MicroChem) was spin-coated on a silicon wafer at 2100 rpm to obtain a thickness of 20 μm prior to UV exposure and development. A PDMS cast of the electrode layer (EL, ~ 4 mm) consisted of three independent 100 μm channels that reduced to 30 μm width and an inter-electrode spacing of 20 μm at the detection region (**Figure 1a**). EL also incorporates all inlet and corresponding outlet ports for molten alloy flow as well as fluid flow. A thin (unpatterned) PDMS sacrificial base layer (SL, ~ 1 mm) was placed under EL to close the channels while taking care to remove all trapped air bubbles between elastomer layers. The flexibility and low surface roughness of polymerized PDMS provided an excellent airtight seal between the layers. The EL+SL assembly was placed on a hot plate at 130 °C for 20 minutes. Molten FM (15 μl, 130 °C, Bombay metal house) was pipetted into the electrode channel inlets
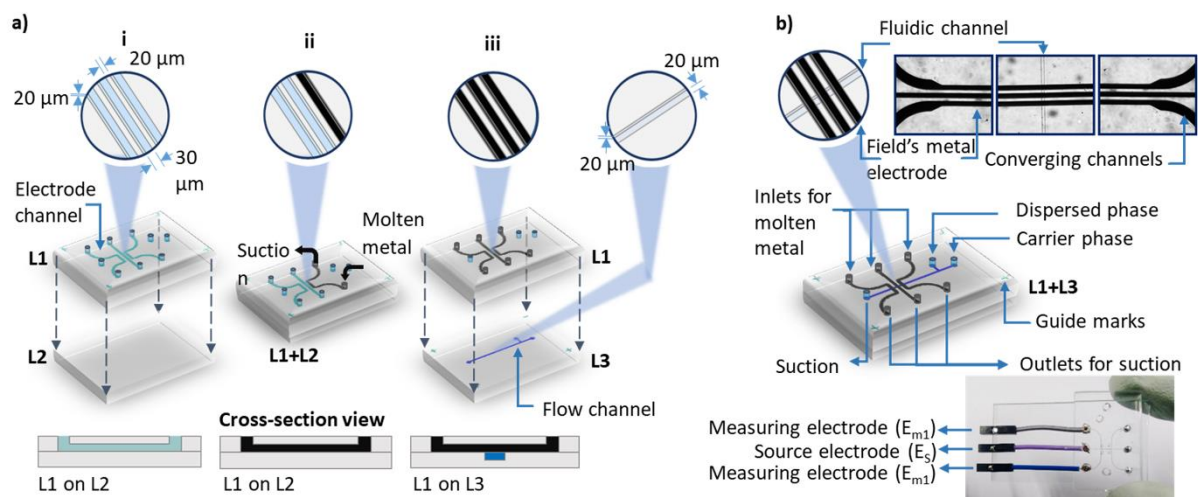
Fig. 1 Coplanar 'in-contact' Field's metal (icFM) electrode fabrication workflow **a)** Schematic of fabrication process; **i**: The PDMS layer containing electrode channels (EL) is placed on a flat PDMS sacrificial layer (SL) which acts as a base during electrode casting. **ii**: Molten FM is flown into the electrode channels using suction. SL is peeled off once the electrodes solidified. **iii:** Electrode layer (EL) is then plasma bonded to the flow layer (FL) **b)** Schematic and optical image of the assembled microfluidic device with embedded coplanar icFM microelectrodes is shown.

3

of the assembly while placed on the hot plate. Using a 50 ml syringe, a suction pressure (~ 80 kPa) was applied to the channel until the metal reached the outlet port for each electrode channel. Suction pressure drives the molten alloy flow through the microchannels as well as holds the two layers together without any additional requirements for bonding. The assembly was allowed to cool after scraping off the excess metal till the FM solidified and then the SL was peeled off to expose the microelectrodes (**Figure 1a**). The flow layer (FL, ~ 1-4 mm) consisted of a 20 µm high and 70 µm wide channel converging to a 20 µm width at the detection region and runs orthogonally to the electrode channels. In case of water-in-oil droplet measurements, a T-junction was added to the flow channel upstream of the detection region. EL and FL were aligned using the guide marks and bonded after a plasma treatment. The bottom layer (FL) was also plasma bonded to a glass slide for device rigidity and ease of operation. To overcome the reduced hydrophobicity of PDMS after plasma treatment, the device was kept overnight at 45 °C (but below the FM melting point, ~ 60 °C). The device thus fabricated, contains a fluidic channel across an array of three 'in-contact' coplanar microelectrodes [**Fig. 1b**].
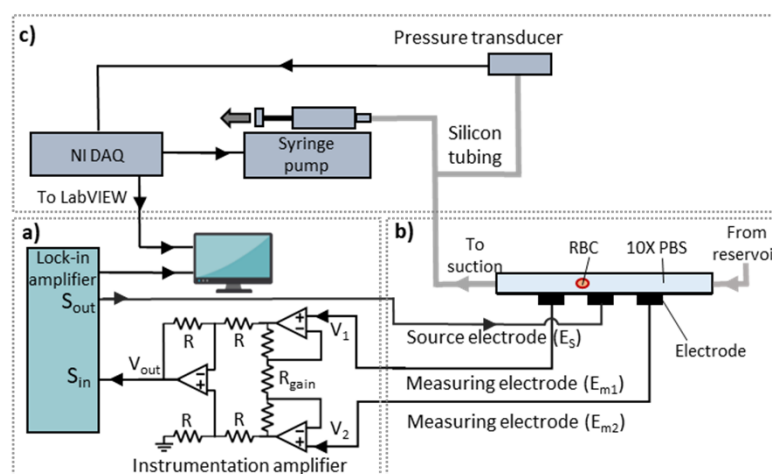
B. Microfluidic Impedance Cytometry setup

A lock-in amplifier with a built-in signal generator was connected to the microelectrodes via a low noise instrumentation amplifier circuit. We used the commonly employed MIC electrode architecture with three coplanar electrodes within the microfluidic chip representing two electrode pairs.[38-40] An excitation AC signal was applied to the source electrode (middle) via the signal-output port of the lock-in amplifier. The two measuring electrodes (on either side) were connected to the instrumentation amplifier circuit [**Fig. 2a**].

Particles passing over the electrodes perturb the dielectric properties (and hence the impedance) of the sample between the electrodes [**Fig. 2b**]. This change is measured as a voltage offset across the two electrode pairs ($\Delta V = |V_2 - V_1|$). The instrumentation amplifier converts the voltage offset (ΔV) into a differential voltage (V_{out}) with a gain ($1 + 2R_{gain}/R$), which was then fed into the signal-input of the lock-in amplifier (either HF2LI, Zurich Instruments or CytoX, MicroX Labs). A software (ZiControl or CytoX) recorded the amplified differential voltage (Vrms) from the lock-in amplifier.

C. Fluidics

Suction pressure was stabilised using a custom-built active-feedback pressure control module. A syringe pump (1010X, New Era) is regulated by A LabVIEW custom code via a NI USB 6008 data acquisition card and MP3V5050V pressure transducer [**Fig. 2c**]. This module controls and stabilises the applied suction pressure in

Fig. 2 Lock-in amplification based Microfluidic Impedance Cytometry (MIC) setup with feedback controlled suction flow
a) Schematic of active feedback pressure control module that regulates suction for fluid flow in the microfluidic channel.
b) Lock-in amplifier with built-in signal generator provides the excitation AC voltage (S$_{out}$) to the source electrode and measures the differential voltage signal (S$_{in}$) from the measuring electrodes via an instrumentation amplifier. **c)** A cross section of the 'in-contact' coplanar electrodes orthogonal to the flow channel with its fluidic and electronic connections

4

real-time by pulling an empty syringe to the set point. This facilitates suction microfluidics for long-term operation of multi-phase microfluidic devices where the flow rate distribution of different phases for the applied suction pressure is regulated by the microchannel geometry.[41] This single pump driven flow-control module significantly reduces the foot print of the whole operation, required reagent volumes and operation costs.

We used a T-junction flow channel architecture for water-in-oil droplet generation.[42] The continuous phase consisted of surfactant stabilised fluorinated oil (Bio-Rad, 1863005) with the cell suspension in 1X Phosphate-buffered saline or PBS (Sigma-Aldrich) as the dispersed phase. The electrolyte concentration was selected to ensure compatibility with potential downstream biochemical reactions and long-term viability of cells in the droplets. The capillary number for the continuous phase and Reynolds number at the T-junction were 8.24×10^{-2} (transient regime) and 0.15, respectively.[42] Droplet volume was ~ 150 pl and generated at a frequency of ~ 10 Hz using 18 kPa suction pressure.

D. Imaging and analysis

The device images were acquired using a brightfield inverted microscope (RAMM, Applied Scientific Instrumentation). High speed fluorescence imaging for particle velocity profiling was done using a sCMOS camera (Orca Flash 4, Hamamatsu) and green fluorescent protein (GFP) expressing *E. coli* cells were used as fluorescent particles. Images were acquired using µManager 2.0.[43] Scanning electron microscope (Ultra 55 FE-SEM, Carl Zeiss) was used for electrode surface micrographs. All the data analysis was done using custom codes in MATLAB.

E. Sample preparation

The blood samples were provided by the author and drawn at the Health center, IISc Bangalore. For erythrocyte enrichment, 5 ml of blood was spun at 500 x g for 7 mins. The supernatant was discarded and the pellet was resuspended in 5 ml of 10X PBS (or 1X PBS in case of droplets). The samples thus prepared were visually inspected using a brightfield microscope [**Supplementary Fig. S1**].

III. RESULTS AND DISCUSSION

Our MIC microfluidic module requires a single standard photolithography workflow to generate two PDMS microchannel layers, i.e. the microelectrode layer (EL) and the flow layer (FL) [**Fig. 1**]. First, the electrodes are fabricated separately by filling the EL microchannels with a fusible alloy (FM). The channel architecture helps define the arrangement, dimensions and the position of the microelectrodes. We chose FM (32.5% Bi, 51% In, 16.5% Sn) among the eutectic fusible alloys because of its non-toxic nature. FM also has a melting point of ~ 60 °C which is significantly above room temperature. The flow and electrode layer (with electrodes placed orthogonal to flow channels) are bonded to finish the icFM device assembly in a cleanroom-free environment thus significantly reducing processing time and resource requirements [**Supplementary Table ST1**]. Deployment of thus fabricated icFM microfluidic device in a MIC setup with an active feedback pressure control module is described in the Methods [**Fig. 2**].

We first confirmed the stability of our feedback pressure control module by monitoring suction pressures of a withdrawn syringe at different set points between 5 to 30 kPa across the flow channel (1 cm x 70 µm x 20 µm) filled with distilled water. We observed a steady pressure drop using our control module (standard deviation ± 0.1 %) as compared to a rapidly decaying pressure difference for a non-feedback operation [**Fig. 3a**]. The linear relationship between the flow velocity at the detection region and the suction pressure applied across our flow channels further confirms the control module's consistency [**Fig. 3b**].

We characterised our icFM microelectrode response (Vrms) for different electrolyte concentrations (0 to 10X PBS) at various AC source frequencies (0.1 – 10 MHz) and peak-to-peak source voltages (0.2 to 2 Vp-p) to optimise the voltage, source frequency and electrolyte concentration for MIC electrode performance. Ideally, the differential voltage (Vrms) between the measuring electrodes should be zero when placed identically on

5
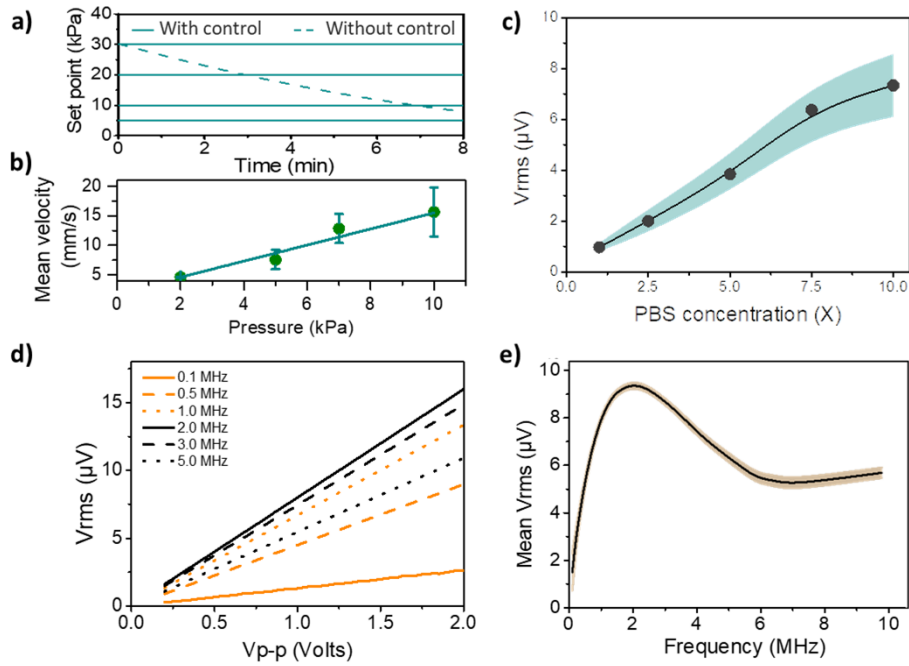
Fig. 3 System characterisation **a)** Suction pressure with and without active feedback pressure control module is plotted with time. **b)** Particle velocity over the electrodes as a function of varying suction pressure across the flow channel. **c)** Output voltage (Vrms) measurement for coplanar icFM electrode as a function of electrolyte (PBS) concentration averaged over different source frequencies (0.1 - 10 MHz) at 2 Vp-p is plotted. **d)** Voltage sweep from 0.2 to 2 Vp-p source voltage performed at various frequencies (0.1 - 5MHz) at 10X PBS is shown. **e)** Mean output voltage (Vrms) for frequency sweep (0.1 - 10 MHz) averaged over source voltages (0.5, 1, 1.5, 2 Vp-p) at 10X PBS is reported.

either sides of the source electrode under similar electrochemical conditions. However, the non-zero differential voltage observed in real-world MIC setups arise from the asymmetry in the electronic system and the system noises and offsets. We relied on the continuity and linearity of the differential signal to evaluate our electrode stability since breakdown in electrode operation will result in discontinuous response. First, we measured the mean Vrms response of the electrodes for electrolyte concentrations from 1X to 10X PBS over a broad frequency range (0.5-10 MHz) at 2 Vp-p. We observed a continuous and monotonically increasing Vrms as a function of electrolyte concentration which suggests that the electrodes are not undergoing electrolysis or corrosion at high saline concentrations [44] [**Fig. 3c**]. Importantly, we observed a linear Vrms output with increasing Vp-p (0- 2 V; 10X PBS) which confirms that these electrodes are electrochemically stable up to 2 Vp-p and the linearity can be extrapolated to even higher source voltages suggesting a wider operable range [**Fig. 3d**]. Using a frequency sweep (0.1 – 10 MHz; at 2 Vp-p and 10X PBS), we observed a continuous but non-linear impedance response [**Fig. 3e**]. This could arise because of capacitive coupling at higher frequencies for our electrodes.[45] Frequency dependence of either the double layer capacitance[46] or instrumentation amplifier gain can also result in such a behaviour.

To demonstrate the icFM microelectrode compatibility with MIC and compare its performance with the popular Pt electrodes (in the same coplanar configuration), we detected human erythrocytes (Red Blood Corpuscles or RBC). A suction pressure of 10 kPa maintained the sample at a mean velocity of ~ 15 mm/sec over the electrodes [**Fig. 3b**] that was optimized for a sampling rate of 7200 Hz. The differential impedance signature of an erythrocyte in the electrolyte as it flows over the microelectrode array is characteristic of a well-described single 'sine-wave' shape in this configuration [**Fig. 4a**].[38] The observed variability in signal peak distribution (as evident from the error bars) arises as a result of variable distance of the flowing cells from the electrodes and inherent cell size dispersity [**Fig. 4b**]. A comparison of icFM and Pt electrodes in equivalent microchannel dimensions demonstrates a marginally higher peak signal variability for icFM electrodes. Nevertheless, the peak

6
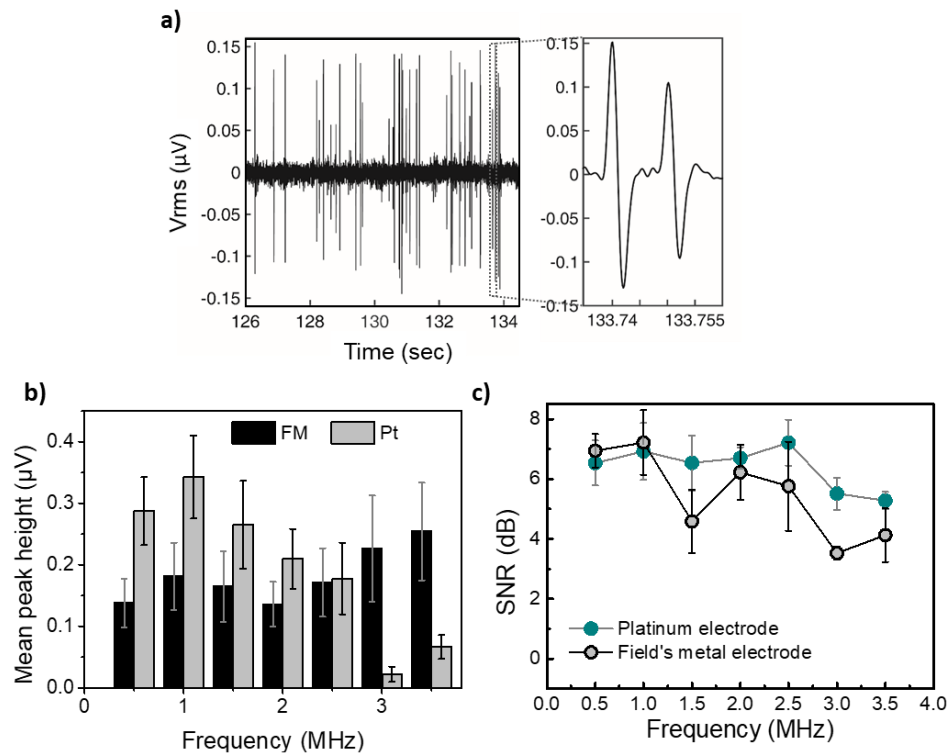
Fig. 4 Single erythrocyte detection with coplanar icFM microelectrode **a)** Differential voltage signal from the icFM MIC setup at 2 Vp-p and 0.5 MHz for flowing dilute suspension of RBC in 10X PBS is shown. (Inset) The observed spikes represent a signature waveform for particle detection in our MIC setup, i.e. each positive-negative peak pair representing a single RBC flowing over the electrodes. **b)** Mean peak heights of differential voltage signal for RBC detection obtained using icFM and platinum electrodes at different frequencies at 2Vp-p source voltage is shown. **c)** Comparison of signal-to-noise ratios (SNR) of icFM and platinum electrodes at different frequencies is plotted.
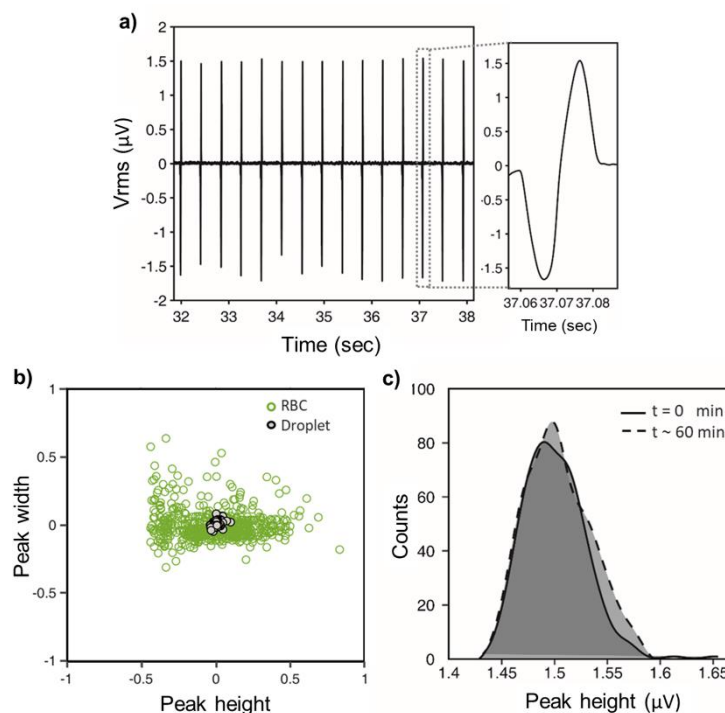
Fig. 5 Water-in-oil droplet detection with icFM microelectrode **a)** Differential voltage signal from MIC setup for droplet detection at 2 Vp-p and 1 MHz is shown. (Inset) A zoomed view of the signature waveform for a single droplet detection is displayed. **b)** Comparison of peak height and corresponding FWHM distribution obtained at 2 Vp-p and 1 MHz for RBC and droplet signals is plotted **c)** Peak height distribution for droplet signals from experiments conducted ~ 60 minutes apart on the same device is shown.

signal values registered by icFM electrodes were comparable to Pt electrodes. While, Pt electrodes displayed a gradual drop in RBC signal over frequencies from 0.5 to 4 MHz, the icFM electrodes were characteristic of a biphasic response with the highest peak signals obtained at 0.5 MHz and 3 MHz. This frequency response is a function of the biophysical and morphological properties of the cell (and subcellular components like vacuoles and nucleus) and can be used for cell classification on the basis of size, cytoplasmic resistance and membrane capacitance.[15] However, we have limited our analysis to cell detection to demonstrate proof-of-principle cell detection capability using icFM electrodes in this study. A comparison of signal-to-noise ratios (SNR) also displayed high SNR for both electrodes over the entire frequency range measured [**Fig. 4c**]. In spite of electrical noises and a comparatively rough surface of solidified alloy over sputtered metal [**Supplementary Fig. S2**], the
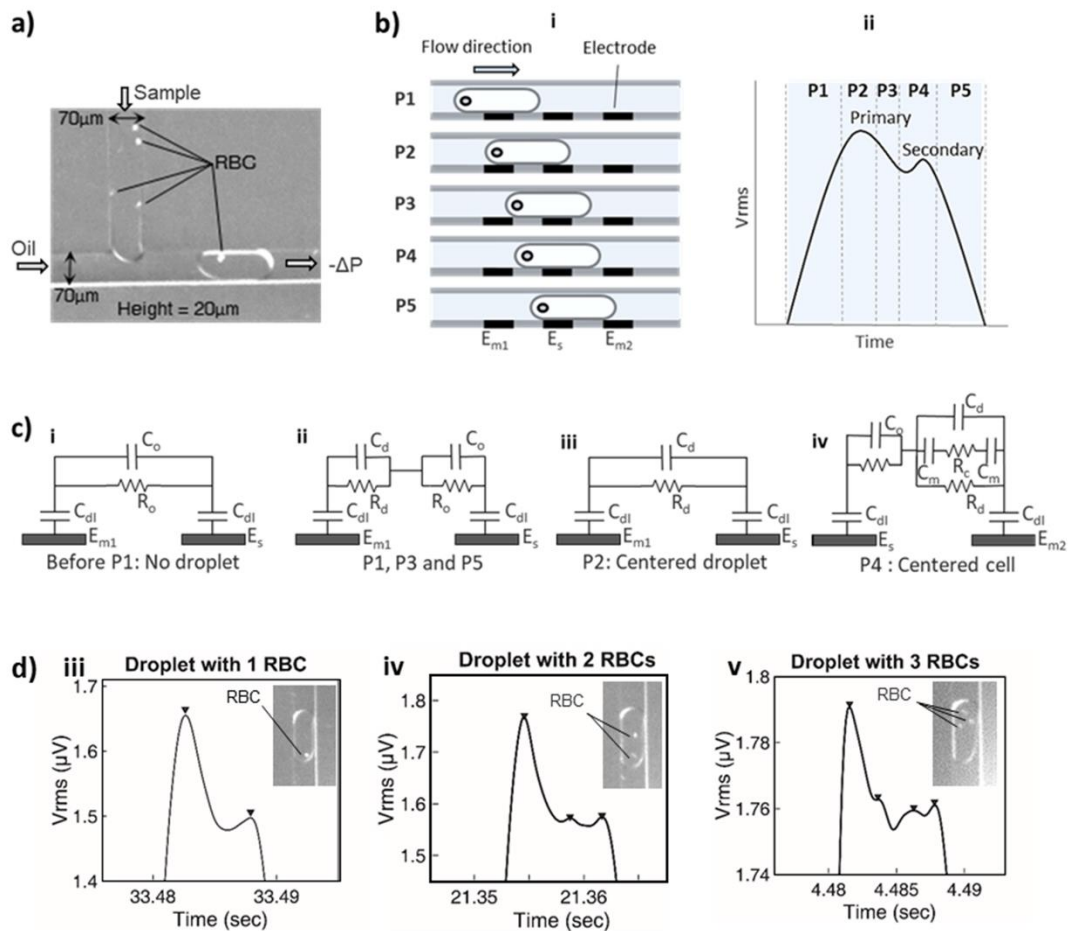

Fig. 6 Cell-in-microdroplet quantification **a)** T-junction microfluidic channel used to encapsulate cell(s) in droplets upstream of the microelectrode array is shown. **b)** Schematic representing evolution of primary and secondary peaks for droplet and cell-in-droplet, respectively is depicted **i:** Droplet (containing a single cell) at specific positions relative to the microelectrode array (E_{m1}, E_{m2}: measuring electrodes, E_s: source electrode) is pictorially shown. **ii:** Contribution of each position to differential signal is schematically plotted (only positive peak of differential signal is considered here, the negative peak carries similar features). **c)** Equivalent electrical circuit model for the droplets at different positions is drawn (C_{dl}: equivalent double layer capacitance due to all interfaces (electrode-oil, oil-electrolyte and electrolyte-electrode); C_o, R_o, C_d, R_d: capacitance and resistance due to oil and droplet respectively; C_m: cell membrane capacitance, R_c: cytoplasmic resistance) **i:** Base impedance without droplet, accounting for low conductivity and dielectric constant of carrier phase (Oil). **ii:** As the aqueous droplet touches E_{m1} (and not E_s), the higher dielectric constant of droplet starts to contribute to the signal. **iii:** Primary peak appears as the droplet touches both the electrodes reaching maximum conductivity and dielectric constant between the electrodes. **iv:** Secondary peak appears as the cell crosses the centre of E_s and E_{m1}. **d)** Differential voltage signal at 2 Vp-p and 1 MHz for droplets carrying cells **i-iii:** Primary peak representing a droplet and secondary peaks representing number of entrapped RBCs is plotted. (Inset) Optical image of different droplets containing as many RBCs is shown.

performance of both electrodes was similar within the accounted parameters. Hence, icFM electrodes can be a viable alternative for MIC based single cell detection.

Next, we integrated icFM electrodes to detect water-in-oil droplets, a common two-phase microfluidic configuration used as micro-reactors.[47] By employing elastomeric walls on all four sides, the microchannels in our devices exhibit uniform hydrophobicity which aids droplet microfluidic operations.[48] Droplets (1X PBS) were generated using a T-junction upstream of the microelectrodes. The signal for aqueous droplets is characteristic of a high dielectric feature in a continuous oil phase flowing through the channel [**Fig. 5a**]. Comparison of the distribution of peak heights and corresponding full width at half maxima or FWHM for erythrocytes and droplets in oil revealed features of the two flow profiles [**Fig. 5b**]. The FWHM is a function of the residence time of the particle in the detection region. A large standard deviation of the FWHM for the RBC (11.7 %) results from the parabolic flow profile within the microchannel. The RBC peak heights have a substantially larger standard deviation (24.7 %) because of the variable normal distance of the cells from the electrodes apart from the inherent cell size heterogeneity and tumbling of the RBC in the channel. On the other hand, droplets show significantly narrow distribution of peak heights (1.9 %) and FWHM (1.8 %) as a result of the plug flow profile of the droplets. The distribution in the droplet signal also agrees well with the polydispersity of the droplet plug length (1.7 %) as calculated using optical methods [**Supplementary Fig. S3**]. We also observed an excellent overlap in the primary peak height distribution for the droplets over time (~ 60 mins) even after continuous measurements on the same device [**Fig. 5c**]. This suggested the long-term stability of the icFM electrodes in such two phase microfluidic systems.

Cell entrapment in droplets is an increasingly popular single cell analysis tool.[49, 50] However, high-throughput quantification of entrapped cells usually relies on high-speed optical imaging. Non-optical methods to detect and quantify cells in microdroplets can aid in challenges with sensitivity and the requirement to label the cells.[34] To demonstrate the applicability of icFM electrodes for quantitative single cell detection in microdroplets, we performed MIC measurements of erythrocytes in droplets [**Fig. 6a**]. We hypothesized that an additional set of secondary signatures superimposed on the droplet signal will be discernible if the droplet contained cell(s) owing to its membrane capacitance [**Fig. 6b**]. Since the cytoplasm is shielded by the low dielectric of the cell membrane at frequencies below 10 MHz, its cytoplasmic conductivity does not contribute to an impedance change in our measurements. Therefore, the cell-in-droplet signal would be defined by a low dielectric feature (cell) suspended in a high dielectric medium (droplet) as its travels in a low dielectric medium (oil). Thus, cells-in-droplets is expected to display a superimposition of the cell signature on the droplet signal resulting in primary and secondary peaks [**Fig. 6b**].[15] The primary and the secondary peak reach their corresponding maxima when the contributor (droplet and cell in droplet, respectively) passes directly over the center of the source and measuring electrode. Superimposition of peaks from entrapped cell(s) while traversing the detection region due to physical overlap which is a low likelihood event, should not contribute to large discrepancies in our peak based analysis. This idea can be further explained by an equivalent electrical circuit model [**Fig. 6c**].[51] The
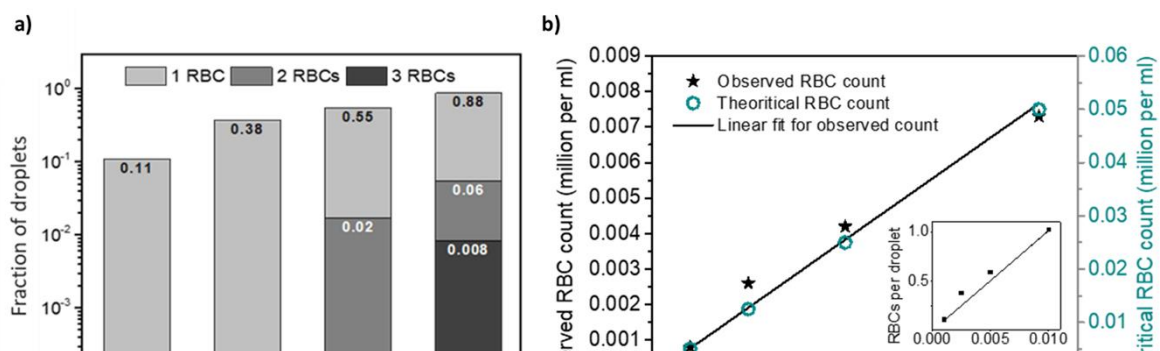
Fig. 7 RBC analysis **a)** Fraction of droplets encapsulating one, two and three RBCs at represented dilutions is plotted. **b)** Comparison between observed and estimates of total RBC count for each dilution factor is plotted. (Inset) Average number of RBC per droplet as a function of increasing dilution factor.

centered droplet would contribute the maximum differential impedance owing to its highest conductivity (1.6 S/m) and relative permittivity (80 for 1X PBS) compared to the carrier phase and the cell [**Fig. 6c**]. The MIC signal for our erythrocytes in droplets indeed displayed secondary peaks consistent with the average number of cells loaded per droplet [**Fig. 6d**]. To statistically validate our cell quantification, we calculated the fraction of droplets with one or more RBC counts from the number of secondary peaks at different dilutions of our erythrocyte suspension [**Fig. 7a**]. The total RBC count for the blood sample was calculated from the average number of RBCs per droplet at respective dilutions. The observed counts at each dilution was consistent with estimates (5 x 10^9 RBCs/ml of human blood) when accounted for the offset attributed to RBC loss during sample preparation [**Fig. 7b**]. This further demonstrated the sensitivity of our icFM microelectrodes for detection of particles in complex two-phase microfluidic systems.

IV.   CONCLUSION

We have demonstrated Field's metal based 'in-contact' (icFM) microelectrodes as a rapid, robust and economical alternative for microfluidic impedance cytometry enabled single cell quantification. We present a technically simple fabrication process that produces highly reproducible microelectrodes in a cleanroom-free environment. Our microelectrodes are stable in all solution conditions used for conventional cell analysis and comparable in performance to state-of-art Pt electrodes. This allows us to monitor cells in water-in-oil droplets non-optically at high rate and sufficient contrast.

Incorporation of non-conductive flow focusing or sheath flow to reduce the detection volume can be further employed with icFM devices to achieve a higher sensitivity.[52, 53] Two opposing icFM electrode layers sandwiching a flow layer in 3D electrode geometry can further improve the MIC signal strength, thus enabling more challenging applications like cell classification and bacteria detection.[15] While our fabricated microelectrodes were designed and characterized for MIC, which places high technical requirements for performance, we also envision their application in AC electrokinetics, electrochemical sensing, microfluidic mixing and sorting.[54-59] As the casting is done directly within the prefabricated devices, the process is compatible with other polymeric materials.[60] With possibility of scaling up the microfabrication process with automation, use of these electrodes in disposable PoC devices can become a reality.

V.   ACKNOWLEDGEMENTS

VI.   REFERENCES

1.   M. Mehling and S. Tay, Current Opinion in Biotechnology **25**, 95-102 (2014).
2.   A. M. Streets, X. Zhang, C. Cao, Y. Pang, X. Wu, L. Xiong, L. Yang, Y. Fu, L. Zhao, F. Tang and Y. Huang, Proceedings of the National Academy of Sciences **111** (19), 7048 (2014).
3.   A. Reece, B. Xia, Z. Jiang, B. Noren, R. McBride and J. Oakey, Current opinion in biotechnology **40**, 90-96 (2016).
4.   W. Jung, J. Han, J.-W. Choi and C. H. Ahn, Microelectronic Engineering **132** (Supplement C), 46-57 (2015).
5.   David J. Beebe, a. Glennys A. Mensing and G. M. Walker, Annual Review of Biomedical Engineering **4** (1), 261-286 (2002).

10

6.   H.A. Stone, a. A.D. Stroock and A. Ajdari, Annual Review of Fluid Mechanics **36** (1), 381-411 (2004).

7.   Q. Shi, L. Qin, W. Wei, F. Geng, R. Fan, Y. Shik Shin, D. Guo, L. Hood, P. S. Mischel and J. R. Heath, Proceedings of the National Academy of Sciences **109** (2), 419-424 (2012).

8.   E. A. Specht, E. Braselmann and A. E. Palmer, Annual Review of Physiology **79** (1), 93-117 (2017).

9.   J. V. Watson, *Introduction to Flow Cytometry*. (Cambridge University Press, Cambridge, 1991).

10.   T. Blasi, H. Hennig, H. D. Summers, F. J. Theis, J. Cerveira, J. O. Patterson, D. Davies, A. Filby, A. E. Carpenter and P. Rees, Nature Communications **7**, 10256 (2016).

11.   M. G. Kim, J. Park, H. G. Lim, S. Yoon, C. Lee, J. H. Chang and K. K. Shung, Scientific Reports **7** (1), 14092 (2017).

12.   H. M. Shapiro, in *Practical Flow Cytometry* (John Wiley & Sons, Inc., 2005), pp. 257-271.

13.   D. Holmes and H. Morgan, Analytical Chemistry **82** (4), 1455-1461 (2010).

14.   M. Hywel, S. Tao, H. David, G. Shady and G. G. Nicolas, Journal of Physics D: Applied Physics **40** (1), 61 (2007).

15.   T. Sun and H. Morgan, Microfluidics and Nanofluidics **8** (4), 423-443 (2010).

16.   N. N. Watkins, U. Hassan, G. Damhorst, H. Ni, A. Vaid, W. Rodriguez and R. Bashir, Science Translational Medicine **5** (214), 214ra170-214ra170 (2013).

17.   X. Han, C. van Berkel, J. Gwyer, L. Capretto and H. Morgan, Analytical Chemistry **84** (2), 1070-1075 (2012).

18.   W. H. Coulter, presented at the Preliminary draft of a talk presented before the National Electronics Conference, Chicago, 1956 (unpublished).

19.   J. S. McGrath, C. Honrado, D. Spencer, B. Horton, H. L. Bridle and H. Morgan, Scientific reports **7** (1), 2601 (2017).

20.   C. E. Chidsey, B. J. Feldman, C. Lundgren and R. W. Murray, Analytical Chemistry **58** (3), 601-607 (1986).

21.   P. K. Kannan, R. V. Gelamo, H. Morgan, P. Suresh and C. S. Rout, RSC Advances **6** (107), 105920-105929 (2016).

22.   Y. Temiz, A. Ferretti, Y. Leblebici and C. Guiducci, Lab on a Chip **12** (22), 4920-4928 (2012).

23.   L. D. Thredgold, D. A. Khodakov, A. V. Ellis and C. E. Lenehan, Analyst **138** (15), 4275-4279 (2013).

24.   A. Sciambi and A. R. Abate, Lab on a Chip **14** (15), 2605-2609 (2014).

25.   C. Clausen, G. Skands, C. Bertelsen and W. Svendsen, Micromachines **6** (1), 110 (2015).

26.   S. Gawad, K. Cheung, U. Seger, A. Bertsch and P. Renaud, Lab on a Chip **4** (3), 241-251 (2004).

27.   J.-H. So and M. D. Dickey, Lab on a Chip **11** (5), 905-911 (2011).

28.   S. H. Song, T. Maleki and B. Ziaie, CMBS **11** (1), 4-5 (2011).

29.   M. T. Guler, I. Bilican, Z. Isiksacan, S. Agan and C. Elbuken, µTAS **8** (3), 3 (2015).

30.   A. L. Richards, M. D. Dickey, A. S. Kennedy and G. D. Buckner, Journal of Micromechanics and Microengineering **22** (11), 115012 (2012).

31.   Q. Zhang, T. Wang, Q. Zhou, P. Zhang, Y. Gong, H. Gou, J. Xu and B. Ma, Scientific Reports **7**, 41192 (2017).

32.   L. Rosenfeld, T. Lin, R. Derda and S. K. Y. Tang, Microfluidics and Nanofluidics **16** (5), 921-939 (2014).

33.   H. N. Joensson and H. Andersson Svahn, Angewandte Chemie International Edition **51** (49), 12176-12192 (2012).

34.   H. Lu, O. Caen, J. Vrignon, E. Zonta, Z. El Harrak, P. Nizard, J.-C. Baret and V. Taly, Scientific Reports **7** (1), 1366 (2017).

35.   C. Song, T. Jin, R. Yan, W. Qi, T. Huang, H. Ding, S. H. Tan, N.-T. Nguyen and L. Xi, Lab on a Chip (2018).

36.   L. F. Thompson, (ACS Publications, 1983).

37.   D. C. Duffy, J. C. McDonald, O. J. A. Schueller and G. M. Whitesides, Analytical Chemistry **70** (23), 4974-4984 (1998).

38.   S. Gawad, L. Schild and P. Renaud, Lab on a Chip **1** (1), 76-82 (2001).

39.   V. Errico, A. D. Ninno, F. R. Bertani, L. Businaro, P. Bisegna and F. Caselli, Sensors and Actuators B: Chemical **247** (Supplement C), 580-586 (2017).

40.   H. C. Clausen, E. G. Skands, V. C. Bertelsen and E. W. Svendsen, Micromachines **6** (1) (2015).

41.   A. R. Abate and D. A. Weitz, Biomicrofluidics **5** (1), 014107 (2011).

42.   J. H. Xu, S. W. Li, J. Tan and G. S. Luo, Microfluidics and Nanofluidics **5** (6), 711-717 (2008).

43.   A. D. Edelstein, M. A. Tsuchida, N. Amodaj, H. Pinkard, R. D. Vale and N. Stuurman, Journal of biological methods **1** (2) (2014).

44.   S. Zeitler, E. Wendler-Kalsch, W. Preidel and V. Tegeder, Materials and Corrosion **48** (5), 303-310 (1997).

45.   W. Shuo, F. C. Lee, D. Y. Chen and W. G. Odendaal, IEEE Transactions on Power Electronics **19** (3), 869-877 (2004).

46.   K. J. Aoki, Journal of Electroanalytical Chemistry **779**, 117-125 (2016).

47.   S.-Y. Teh, R. Lin, L.-H. Hung and A. P. Lee, Lab on a Chip **8** (2), 198-220 (2008).

48.   B. Subramanian, N. Kim, W. Lee, D. A. Spivak, D. E. Nikitopoulos, R. L. McCarley and S. A. Soper, Langmuir **27** (12), 7949-7957 (2011).

49.   H. N. Joensson and H. Andersson Svahn, Angewandte Chemie International Edition **51** (49), 12176-12192 (2012).

50.   M. T. Guo, A. Rotem, J. A. Heyman and D. A. Weitz, Lab on a Chip **12** (12), 2146-2155 (2012).

51.   D. Holmes, D. Pettigrew, C. H. Reccius, J. D. Gwyer, C. van Berkel, J. Holloway, D. E. Davies and H. Morgan, Lab on a Chip **9** (20), 2881-2889 (2009).

52.   R. Rodriguez-Trujillo, C. A. Mills, J. Samitier and G. Gomila, Microfluidics and Nanofluidics **3** (2), 171-176 (2007).

53.   C. Bernabini, D. Holmes and H. Morgan, Lab on a Chip **11** (3), 407-412 (2011).

54.   N. Sasaki, T. Kitamori and H.-B. Kim, Lab on a Chip **6** (4), 550-554 (2006).

55.   J. Luo, E. L. Nelson, G. P. Li and M. Bachman, Biomicrofluidics **8** (3), 034105 (2014).

56.   M. Z. Bazant and T. M. Squires, Physical Review Letters **92** (6), 066101 (2004).

57.   A. Ramos, H. Morgan, N. G. Green and A. Castellanos, Journal of Physics D: Applied Physics **31** (18), 2338 (1998).

58.   Z. Nie, C. A. Nijhuis, J. Gong, X. Chen, A. Kumachev, A. W. Martinez, M. Narovlyansky and G. M. Whitesides, Lab on a Chip **10** (4), 477-483 (2010).

59.   D. Chatterjee, H. Shepherd and R. L. Garrell, Lab on a Chip **9** (9), 1219-1229 (2009).

60.   B. Zhang, Q. Dong, C. E. Korman, Z. Li and M. E. Zaghloul, Scientific Reports **3**, 1098 (2013).